Probabilistic Small-signal Stability Assessment and Cooperative Control for Interconnected Microgrids via Back-to-back Converters

Yuhong Wang, *Senior Member*, *IEEE*, Xinyao Wang, *Student Member*, *IEEE*, Jianquan Liao, *Member*, *IEEE*, Miaohong Su, *Student Member*, *IEEE*, and Yongyue Liu

***Abstract*—The flexible interconnection of microgrids (MGs) adopting back-to-back converters (BTBCs) has emerged as a new development trend in the field of MGs. This approach enables larger-scale integration and higher utilization of distributed renewable energy sources (RESs). However, their stability characteristics are very different from single MG due to the control characteristics of flexible interconnection. Meanwhile, the uncertainty and stochastic dependence structures of RESs and loads create challenges for stability analysis and cooperative control. In this paper, a probabilistic small-signal stability assessment and cooperative control framework is proposed for interconnected MGs via BTBCs. First, a cooperative control architecture for MGs is constructed. Then, a small-signal model of interconnected MGs via BTBCs containing primary control and secondary control is developed. This model facilitates the analysis of the impacts of BTBCs and various control strategies on the system stability. Subsequently, Copula functions and polynomial chaos expansion (PCE) are combined to achieve the probabilistic small-signal stability assessment. On this basis, the parameters of the cooperative control are optimized, enhancing the robustness of interconnected MGs via BTBCs. Finally, a case of interconnected MGs via BTBCs are built in MATLAB/Simulink to verify the accuracy and effectiveness of the proposed framework.**

***Index Terms*—Back-to-back converter (BTBC), interconnected microgrid, uncertainty, small-signal stability, cooperative control.**

I. Introduction

MICROGRID (MG) is an effective way to achieve the flexible consumption and efficient application of renewable energy sources (RESs) [1]. However, the ability of a single MG to absorb large-scale RESs is limited due to its capacity and inertia [2]. With the reduced costs of voltage source converters (VSCs), the flexible interconnection of back-to-back converters (BTBCs) has become one of the favored solutions for integrating multiple MGs [3]. The interconnection of BTBCs enables MG connections across different feeders, districts, or voltage levels. It facilitates the access of a high proportion of distributed RESs and loads with broad application prospects [4]. However, the nonlinear characteristics of interconnected MGs (IMGs), coupled with the unpredictability of RESs and fluctuating loads, present challenges in stability analysis and cooperative control.

Current research on MG small-signal stability mainly focuses on isolated MGs and those interconnected through AC links. Reference [5] developed a state-space model for VSCs, but only assessed the effects of droop control. References [6] and [7] analyzed the influence of droop and local controls on the MG stability. However, these works ignored the impact of the secondary control and the fluctuation of RESs. Reference [8] introduced the secondary control and discovered new oscillatory modes that could destabilize MG clusters. However, there are few relevant stability analyses for interconnection methods. In summary, most existing literature does not consider the impact of cooperative control, interconnection methods, or fluctuations of RESs on the stability.

Deterministic methods for small-signal stability analysis no longer meet the research needs. Therefore, probabilistic small-signal stability analysis methods, which consider the variability of operational parameters, have been widely used in recent years. The main methods for probabilistic small-signal stability analysis in power systems include simulation methods [9], analytical methods [10], and approximation methods [11], [12].

Among them, polynomial chaos expansion (PCE) [13]-[15] has been widely applied in various fields of power systems due to its robust mathematical foundation as well as its accuracy and efficiency. However, different uncertainties from loads and RESs exhibit high degrees of nonlinear and non-Gaussian stochastic dependencies (or correlations). This affects the effectiveness of probabilistic analysis methods [16]. One effective method to address correlations is the Copula-based methods [17]-[19]. Reference [20] adopted a combination of copulas and PCE (Co-PCE) to address the effects of correlations and randomness in probabilistic load

Manuscript received: April 28, 2024; revised: June 17, 2024; accepted: August 28, 2024. Date of CrossCheck: August 28, 2024. Date of online publication: September 19, 2024.

This work was supported by the National Key R&D Program of China "Response-driven intelligent enhanced analysis and control for bulk power system stability" (No. 2021YFB2400800).

Y. Wang, X. Wang, J. Liao (corresponding author), M. Su, and Y. Liu are with the College of Electrical Engineering, Sichuan University, Chengdu, China (e-mail: yuhongwang@scu.edu.cn; xinyao@stu.scu.edu.cn; jquanliao@scu.edu.cn; sumiaohong9@163.com; lyymoon@163.com).

DOI: 10.35833/MPCE.2024.000449

flow calculations in power systems. Reference [21] applied the same combination to analyze the impact of different correlation modeling techniques on load flow calculation results. These studies focus on probabilistic load flow issues, while BTBC-IMGs not only consider uncertainties and dependencies but also consider the impact of cooperative control schemes and control parameters on stability assessment.

The cooperative control of BTBC-IMGs aims to address the challenge of achieving equitable active power distribution based on capacity ratios at the cluster level. Existing methods can be classified into two categories: those that do not rely on the communication network and those that do. Without relying on communication network interactions, [22] and [23] suggested an active power-voltage-frequency (*P-V-f*) droop control method. Reference [24] proposed that active/reactive power transmission commands can be obtained by extracting frequency and voltage deviation signals. However, these control methods involve proportional adjustments and are unable to achieve objectives such as frequency/voltage restoration without difference and equitable active power sharing among MGs. References [25] - [27] showed that hierarchical distributed control models can be adapted for interconnected AC and DC MGs. However, these methods struggle to achieve coordinated control of multiple objectives such as frequency, voltage, and power, and do not account for the impacts associated with uncertainties of RESs.

In summary, there is an interaction between cooperative control and probabilistic small-signal stability, which restrict the application of IMGs. Therefore, this paper develops a probabilistic small-signal stability assessment and cooperative control framework. The main contributions of this paper are as follows.

1) A cooperative control architecture for BTBC-IMGs is constructed, which enhances the accuracy of frequency and voltage recovery and power equalization. On this basis, a small-signal model of BTBC-IMGs considering cooperative control is built, which can analyze the impact of different control strategies and BTBCs on the stability of IMGs.

2) The probabilistic small-signal stability assessment for BTBC-IMGs is developed based on Co-PCE. The instability risk of BTBC-IMGs is evaluated. Considering the correlation and uncertainty, the impact of RESs and cooperative control on the damping response surface is investigated. Meanwhile, the effects of different interconnection and control on the stability of BTBC-IMGs are analyzed.

3) Combined with stability assessment results, the cooperative control parameters are optimized, which enhances the robustness of BTBC-IMGs. The cooperative control of the frequency, voltage, and power of IMGs is realized under a high proportion of RES integration.

The rest of this paper is organized as follows. Section II establishes the small-signal model and the cooperative control for BTBC-IMGs. Section III presents Co-PCE for probabilistic small-signal stability assessment. Section IV exhibits the proposed probabilistic small-signal stability assessment and cooperative control framework. Section V validates the effectiveness of the proposed framework by triple-ended IMGs. Section VI presents the conclusion of this paper.

II. Small-signal Model and Cooperative Control for BTBC-IMGs

A. Cooperative Control Architecture and Objective

Figure 1 shows a general structure of the BTBC-IMGs, which mainly consists of b MGs, $2d$ interlinking lines (ILs), and d BTBCs. In Fig. 1, PLL stands for phase-locked loop; PCC stands for point of common connection; and DG stands for distributed generation. The MGs can have different structures with any number of DGs, loads, and lines, which are interconnected by BTBCs and AC/DC ILs. In this paper, each MG unit contains a DGs, c ILs with the grid connection point, and a centralized equivalent ZIP load.

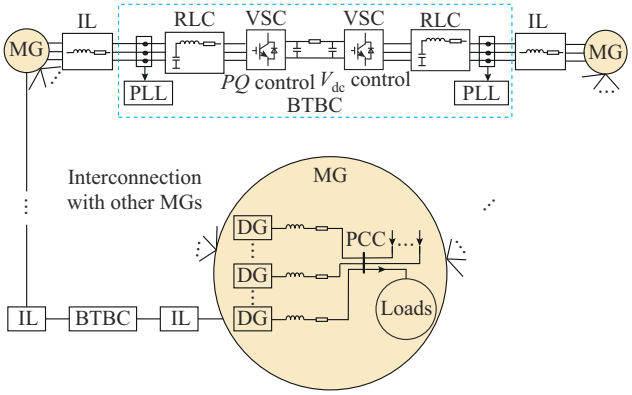

Fig. 1. General structure of BTBC-IMGs.

A two-level cooperative control architecture is designed to take over the control responsibility of MGs in both individual and interconnected operating modes. In the first control level, neither the MGs nor the BTBCs require communication, while in the second control level, communication is required, as shown in Fig. 2.

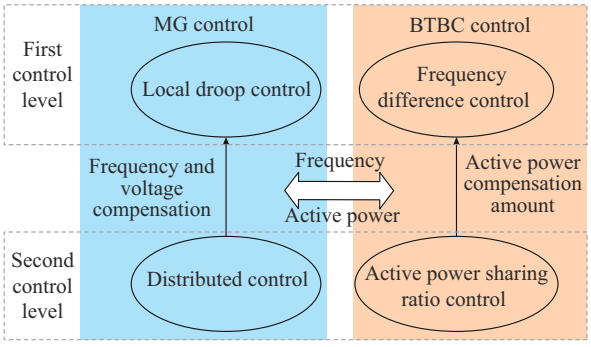

Fig. 2. Cooperative control architecture of BTBC-IMGs.

The first control level comprises the local droop control and frequency difference control. The objectives of voltage stability, frequency stability, active power sharing, and reactive power sharing in DGs are fulfilled in the first control level. The secondary control level is mainly responsible for accurately restoring the voltage and frequency to rated values and improving the power sharing in IMGs.

The most common control architectures for the second control level are centralized and distributed types, where communication links are used to share the data among DGs. In

the second control level, the distributed control based on consistency algorithms is employed to realize frequency and voltage recovery within the MG, as well as precise power sharing. BTBC control is designed based on the difference in active power ratio of MG, to achieve equal distribution of active power between MGs. The communication topology of BTBC-IMGs is shown in Fig. 3. BTBC communicates with the master controller in each MG. The master controller then distributes the instructions to slave controllers.

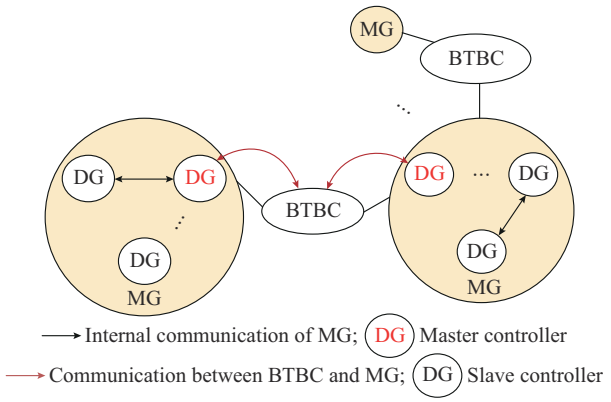

Fig. 3. Communication topology of BTBC-IMGs.

The control objectives include frequency and voltage recovery with zero difference and global accurate active power sharing in the BTBC-IMGs. The specific control objectives are as follows.

1) Objective 1: secondary frequency recovery control of each DG within MGs to maintain the frequencies at the rated value.

2) Objective 2: secondary voltage recovery control of each DG within MGs to restore the voltages to the rated values.

3) Objective 3: equalization of active power among DGs in MGs, so that each DG could output according to its active capacity.

4) Objective 4: equalization of reactive power among DGs in MGs, so that each DG could output according to its reactive capacity.

5) Objective 5: active power sharing ratio control between MGs in the BTBC-IMGs, which controls the active power transmission of each BTBC to balance the output of each MG according to the equivalent droop coefficient.

B. Model of BTBC-IMGs

The MGs established in this paper include photovoltaic (PV), wind turbine, and load models. The randomness and correlation of power generation units and loads lead to uncertainty in the power fluctuations of the system. The comprehensive ZIP load model is used, which can correspond to various load types in the MG.

The control system of DGs consists of droop control and power sharing control for voltage and current. The droop control simulates the active and reactive power droop characteristics of the synchronous generator. The power sharing control is developed by the control of output current and voltage. The PV array of the PV system is described by an engineering model of the PV module, which is based on a linear approximation [20]. The state space model of doubly-fed wind turbines is constructed based on [11].

According to Fig. 4, a BTBC can be controlled by two controllers to exchange power between two MGs. Subscripts i and j represent the variables of VSC_i and VSC_j, respectively. Subscripts d and q represent the variables in the dq coordinate system. Subscripts min and max represent the minimum and maximum values of corresponding variables, respectively. The internal power controller of VSC_i receives the rated active and reactive power references P_{ref} and Q_{ref} and uses current control to control BTBC power exchange. The DC voltage controller of VSC_j receives the DC voltage reference $v_{\mathrm{dc,ref},j}$ and uses a constant DC-side voltage control as the voltage support for the DC transmission. $i_{d\mathrm{ref}}$ and $i_{q\mathrm{ref}}$ are the current reference values. v_{dc} and v_{fc} are the DC voltage and AC voltage, respectively. i_{fc} is the AC current. L_{fc} is the AC-side inductance. ω_{B} is the output angular frequency of PCC. m is the control signal of pulse width modulation. PI stands for proportional-intergral.

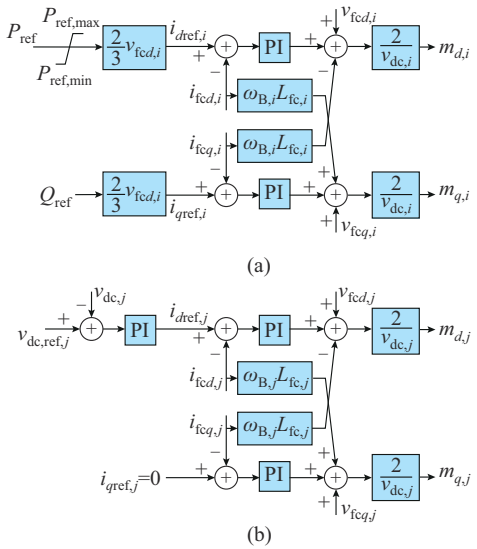

Fig. 4. BTBC control section. (a) Internal power control of VSC_i. (b) DC voltage control of VSC_j.

The internal power controller receives the active and reactive power references from the active power transmission command and aims to exchange scheduled power by controlling the VSC current. Meanwhile, the DC voltage control stabilizes the DC-side voltage by controlling the VSC. In addition, two PLLs are required for the VSCs to synchronize with the MGs. In addition, the power part comprises two AC sides and one common DC link. A dynamic model of a BTBC consists of AC and DC sides, power control, DC voltage control, and PLLs.

By modeling IMG modules separately, it is possible to model various IMG structures with any number of MGs. The IMG state space can be represented as:

$$\dot{\boldsymbol{X}}_{\mathrm{IMG}} = \boldsymbol{A}_{\mathrm{IMG}} \boldsymbol{X}_{\mathrm{IMG}} \tag{1}$$

where $\boldsymbol{X}_{\mathrm{IMG}}$ contains $(13a+2)b+2c+21d$ state variables; and $\boldsymbol{A}_{\mathrm{IMG}}$ is the $(13a+2)b+2c+21d$ order matrix.

C. Cooperative Control

The control strategies are divided into MG control and BTBC control [27]. In the first control level of MG control, each DG adopts the local droop control to quickly respond to various disturbances. In the second control level of MG control, each DG adopts distributed control. It achieves frequency and voltage regulation within the MG (Objectives 1 and 2), as well as equalization of active and reactive power between MGs (Objectives 3 and 4). The derivation of frequency, voltage, active power, and reactive power recovery control can be found in Appendix A. The key parameters of distributed control within the MG include the frequency compensation gain C_ω, active power compensation gain C_P, voltage compensation gain C_v, and reactive power compensation gain C_Q.

In BTBC control, each BTBC adopts frequency difference control to achieve flexible power transmission. The specific control is expressed as:

$$P_{\text{ref}} = K_{p\text{BP}}(\omega_k - \omega_s) + K_{i\text{BP}}\int(\omega_k - \omega_s)\text{d}t \tag{2}$$

where $K_{p\text{BP}}$ and $K_{i\text{BP}}$ are the proportional and integral adjustment coefficients of the P_{ref} controller, respectively; and ω_k and ω_s are the frequencies on both sides of BTBC.

The secondary control of BTBC obtains the active power ratio of MGs on both sides of BTBC through communication, thereby achieving global active power sharing control (Objective 5). The specific control is expressed as:

$$P_{com} = K_{p\text{B}\alpha}(\alpha_k - \alpha_s) + K_{i\text{B}\alpha}\int(\alpha_k - \alpha_s)\text{d}t \tag{3}$$

where P_{com} is the output of the active power sharing ratio control; $K_{p\text{B}\alpha}$ and $K_{i\text{B}\alpha}$ are the proportional and integral adjustment coefficients of the P_{com} controller, respectively; and α_k and α_s are the active power ratios on both sides of BTBC. Therefore, the BTBC control can be written as:

$$P_{\text{ref}} = K_{p\text{BP}}(\omega_k - \omega_s) + K_{i\text{BP}}\int(\omega_k - \omega_s)\text{d}t + P_{com} \tag{4}$$

The key parameters of BTBC control include $K_{p\text{BP}}$, $K_{i\text{BP}}$, $K_{p\text{B}\alpha}$, and $K_{i\text{B}\alpha}$.

III. Co-PCE

A. Stochastic Dependence of Wind, PV, and Load

Geographically close RESs and loads have correlated dependence. This would result in the loss of independence of random variables, or the random variables no longer adhere to a standard normal distribution. Therefore, this subsection addresses the correlation of random variables based on Copula function.

1) Stochastic Distribution of Wind, PV, and Load

According to historical data recorded by the National Renewable Energy Laboratory (NREL) [28], different cities exhibit different distribution characteristics of wind power and illumination intensity. Figure 5 displays the probability density functions (PDFs) of the illumination intensity and load at a certain time. The actual distribution exhibits obvious multi-peak characteristics, making it difficult for standard distribution models to accurately depict these characteristics. Therefore, the non-parametric kernel density estimation is used for analysis [18].

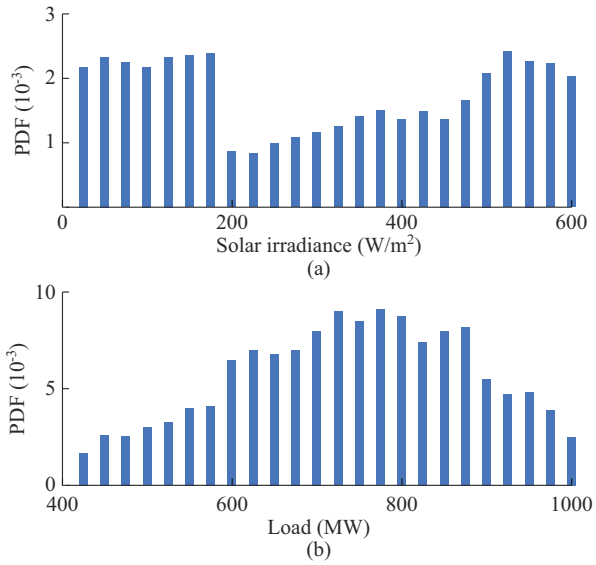

Fig. 5. PDFs of solar irradiance and load at a certain time. (a) Illumination intensity. (b) Load.

Based on the non-parametric kernel density estimation, the marginal probability distributions of wind turbines 1 and 2 in the same wind farm are obtained, as shown in Fig. 6. The kernel distribution estimate is a result of the kernel density estimation method. The empirical distribution function approximates the actual distribution function, which can be used to judge the accuracy of the estimation. The non-parametric estimates are not the same as the empirical distribution function, but the differences are small.

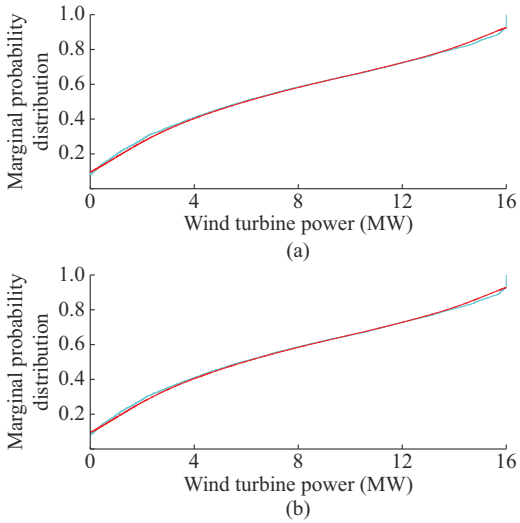

Fig. 6. Marginal probability distribution of wind turbines. (a) Wind turbine 1. (b) Wind turbine 2.

2) Correlation Processing

The correlation among wind speed, PV, and load variables is calculated based on Pearson linear correlation coefficient and Kendall rank correlation coefficient τ. When the absolute value of the correlation coefficient is greater than the threshold η (in this paper, η is set to be 0.45), the variables

are strongly correlated. Otherwise, they are considered weakly correlated. The Copula theory is adopted to establish a joint PDF for strongly correlated variables, and a univariate PDF is established for weakly correlated variables.

According to Sklar's theorem, the joint distribution function $F(\cdot)$ can be converted into the marginal distribution function $f_i(\cdot)$ of each component of the random variable, and a Copula function $C(\cdot)$ that describes the correlation of N random variables, expressed as:

$$F(x_1, x_2, \ldots, x_N) = C(f_1(x_1), f_2(x_2), \ldots, f_N(x_N)) \tag{5}$$

where x_i $(i = 1, 2, \ldots, N)$ is the input variable. The estimate of the cumulative distribution function (CDF) for x_i is:

$$\hat{z}_i = \int_{-\infty}^{x_i} \hat{f}_h(x_i)\mathrm{d}x_i \tag{6}$$

where $\hat{f}_h(\cdot)$ is the estimated value of the PDF.

The selection of an appropriate Copula function is contingent upon the calculation of the optimal Copula function. The empirical Copula function that defines the sample is as follows:

$$\hat{C}_n(z_1, \ldots, z_i, \ldots, z_N) = \frac{1}{n} I(F_1'(x_1) \le z_1, \ldots, F_i'(x_i) \le z_i, \ldots, F_N'(x_N) \le z_N) \tag{7}$$

where $F_i'(\cdot)$ is the empirical distribution function; n is the number of random variables in the empirical distribution function; $I(\cdot)$ is the schematic function; and z_i is the CDF. The squared Euclidean distance between the empirical Copula function and the theoretical Copula function is as follows:

$$d_s^2 = \sum_{i=1}^{n} \left| \hat{C}_n(z_1, \ldots, z_i, \ldots, z_N) - \hat{C}(z_1, \ldots, z_i, \ldots, z_N) \right|^2 \tag{8}$$

where $\hat{C}(\cdot)$ is the theoretical Copula function.

The theoretical Copula function with the shortest distance is selected as the optimal Copula function. The squared Euclidean distance between five typical Copula functions and the empirical Copula function is shown in Fig. 7. Since the squared Euclidean distance between the t-Copula function and the empirical Copula function is the shortest, the t-Copula function is selected as the optimal Copula function for the correlation modeling.

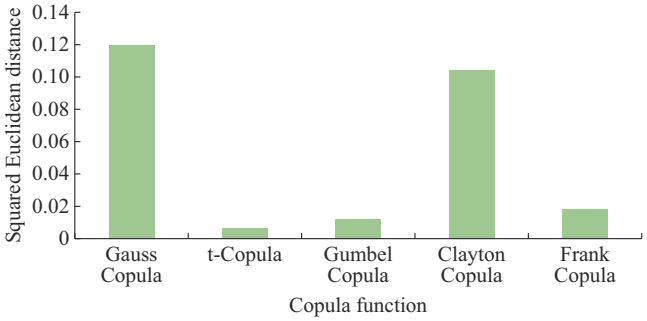

Fig. 7. Squared Euclidean distances between typical Copula functions and empirical Copula function.

B. PCE

PCE is a widely used method for uncertainty quantification in different fields [19]. By representing random variables or processes with orthogonal polynomials, PCE can provide analytical computation of model response statistics. Suppose that Y is the model response (i.e., system responses such as damping ratio), it can be represented by a polynomial function of input random vector $\boldsymbol{X}$ as:

$$Y = \sum_{i=1}^{\infty} a_i \Psi_i(\boldsymbol{X}) \tag{9}$$

where a_i and Ψ_i are the orthogonal basis and its corresponding coefficient with respect $\boldsymbol{X}$, respectively.

The PCE model assumes that the input vector is independent. After Copula correlation modeling and matrix transformation, the dependent input random vector $\boldsymbol{X}$ is transformed into an independent input random vector $\boldsymbol{U}$ [20]. PCE constructs the model of the relationship between $\boldsymbol{U}$ and model response that captures the nonlinear dependence while maintaining the orthogonality of basis. For the damping ratio ξ, the PCE model is constructed as:

$$\xi = c_0 H_0 + \sum_{i_1=1}^{\infty} c_{i_1} H_1(U_{i_1}(\theta)) + \sum_{i_1=1}^{\infty} \sum_{i_2=1}^{i_1} c_{i_1} c_{i_2} H_2(U_{i_1}(\theta), U_{i_2}(\theta)) + \sum_{i_1=1}^{\infty} \sum_{i_2=1}^{i_1} \sum_{i_3=1}^{i_2} c_{i_1} c_{i_2} c_{i_3} H_3(U_{i_1}(\theta), U_{i_2}(\theta), U_{i_3}(\theta)) + \ldots \tag{10}$$

where θ denotes a random variable; c_{i_k} $(k = 0, 1, 2, \ldots)$ is the PCE coefficient; and $H_k(\cdot)$ $(k = 0, 1, 2, \ldots)$ is the k-order Hermite polynomial, which is a function of the multi-dimensional standard normal random variables U_{i_k}. $\boldsymbol{X}$ in the original space is processed by correlation modeling as a function of variables that adhere to a standard normal distribution.

The k-order Hermite polynomial is:

$$H_k(U_{i_1}, U_{i_2}, \ldots, U_{i_k}) = \mathrm{e}^{\boldsymbol{U}^{\mathrm{T}}\boldsymbol{U}/2} (-1)^k \frac{\partial^k}{\partial U_{i_1} \partial U_{i_2} \ldots \partial U_{i_k}} \mathrm{e}^{-\boldsymbol{U}^{\mathrm{T}}\boldsymbol{U}/2} \tag{11}$$

Equation (10) adopting finite p-order Hermite PCE will have N_a unknown constants with N_a equals:

$$N_a = \frac{(k+p)!}{k!p!} \tag{12}$$

The truncated equation is:

$$\xi = \sum_{i=0}^{p} \hat{c}_i H_i(\boldsymbol{U}) \tag{13}$$

where $\hat{c}_i$ denotes the set of c_{i_k} $(k = 0, 1, 2, \ldots)$. To solve the surrogate model of the system output, the probability allocation point method is utilized to evaluate $\hat{c}_i$. First, select Q combination points for $\boldsymbol{U}$. The selected points need to cover high-probability areas, such as the origin and points near the origin. The $(p+1)^k$ coordination points from the roots of the Hermite polynomial of order $p+1$ are obtained to form a symmetrical coordination point. According to the PCE series, symmetrical coordination points are selected to generate the corresponding Hermite polynomials. The matrix $\boldsymbol{H}$ is an $N \times N_a$ space-independent matrix, consisting of known Hermite polynomials computed at the selected N sets of collocations. The calculation ends when the matrix $\boldsymbol{H}$ reaches full rank. This method for selecting coefficients improves the computational efficiency and estimation accuracy of PCE coefficients, thereby improving the performance of the uncertainty analysis.

IV. Proposed Probabilistic Small-signal Stability Assessment and Cooperative Control Framework

The flow chart of probabilistic small-signal stability assessment and cooperative control of the BTBC-IMGs is shown in Fig. 8. It can be divided into three steps, i.e., preparation, polynomial construction, and small-signal stability assessment and parameter optimization.

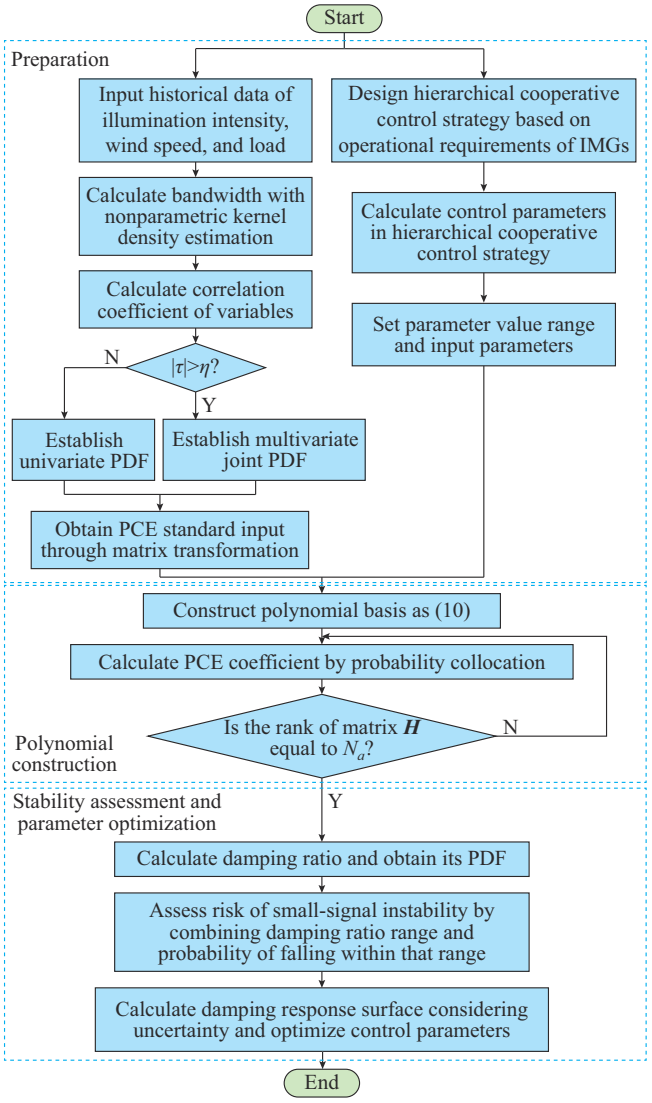

Fig. 8. Flow chart of probabilistic small-signal stability assessment and cooperative control of BTBC-IMGs.

Firstly, wind speed, illumination intensity, and load data are modeled relevantly, and parameters are designed for the cooperative control of the BTBC-IMGs. Secondly, the weak damping ratio is chosen as the polynomial output and the display expression between the damping ratio and multiple input variables is constructed. This assesses the small-signal stability of the BTBC-IMGs and quantifies the extent to which the parameters affect the stability. The parameter optimization is further implemented to enable the system to maintain an accurate control objective despite the consideration of uncertainty fluctuations.

V. Simulation

The case of the BTBC-IMG is built in MATLAB/Simulink. The key mode damping ratio of the system is selected as an evaluation index for small-signal stability to evaluate the stability probability of the BTBC-IMG that contains RESs and loads. This case includes MG_1, MG_2, and MG_3 interconnected by $BTBC_1$, $BTBC_2$, and $BTBC_3$, as shown in Fig. 9. One MG contains a DG, two wind turbines, and two PVs, named as DG_j ($j=1,2,3,4,5$). The load is represented by an equivalent ZIP load and connected in parallel at a PCC. The random input variables include illumination intensity, wind speed, MG control parameters C_ω and C_Q, and BTBC control parameters $K_{i\mathrm{BP}}$ and $K_{i\mathrm{B}\alpha}$.

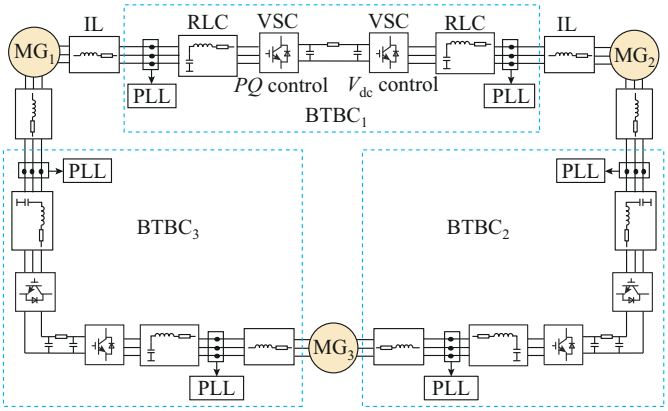

Fig. 9. Structure of BTBC-IMG.

A. Stability Assessment

1) Stability Assessment Considering Relevant Uncertainties

The historical data come from NREL in the United States [28]. The correlation among the load, wind turbine, and PV is calculated, and the results with the highest degree of correlation are selected for correlation modeling. The correlation coefficient calculation indicates a strong correlation between the two wind turbines and between the two PVs. The correlations between the loads, between the loads and wind turbines, and between the loads and PVs are relatively weak.

The basic data of this case are shown in Table I. The pair of conjugate eigenvalues closest to the imaginary axis is selected as the key eigenmode, and the corresponding damping ratio is 0.04. The Co-PCE is adopted to evaluate the probability of system stability.

Figure 10 shows the damping ratio results obtained from the Co-PCE and modal analysis after adopting the Copula-based correlation modeling. The results obtained from the modal analysis can be considered as the true value of the damping ratio. The points in Fig. 10(b) are arranged linearly with a trend of slope 1. Therefore, the Co-PCE can accurately estimate the damping ratio in a series of random scenarios generated by random wind speed, illumination intensity, and load.

The order of Hermite PCE is three, and Co-PCE is applied to calculate the probability of system stability. The stochastic response surface method (SRSM) without considering the nonlinear correlation [16] is selected for comparison. SRSM is one of the types of PCE, constructed using Her-

mite polynomials.

TABLE I
POWER AND CONTROL DATA OF STUDIED CASE

Parameter	Value
Droop coefficients of DG_1, DG_2, DG_3, DG_4, DG_5,	3.2, 4.8, 4.8, 6.4, 6.4
Proportional and integral parameters of DG voltage controller	0.005, 20
Proportional and integral parameters of DG current controller	30, 500
Proportional and integral parameters of BTBC current controller	20, 200
Proportional and integral parameters of BTBC voltage controller	2, 20
Proportional and integral parameters of BTBC PLL	0.4, 4
BTBC resistance, inductance, and capacitance	0.05 Ω, 2 mH, 100 μF
DC capacitance and resistance	400 μF, 0.05 Ω

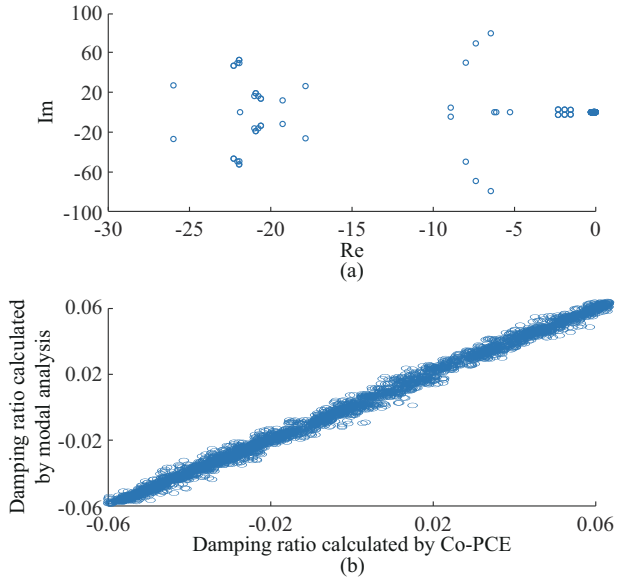

Fig. 10. Accuracy verification of Co-PCE. (a) Characteristic roots from modal analysis. (b) Damping ratio obtained from Co-PCE.

The PDF and CDF calculated by comparing the Co-PCE, SRSM, and Monte Carlo (MC) method are shown in Fig. 11. It is obvious that the results of Co-PCE are more accurate than those of SRSM due to the accurate correlation modeling of random inputs. The calculation results of SRSM are poor due to inaccurate PDFs of illumination intensity and wind speed. The instability probability estimated by Co-PCE is 32%, which has a high degree of coincidence with that of MC method.

To further quantitatively verify the accuracy of the results obtained by Co-PCE, the mean square error coefficient ε_{ARMS} and the relative average error coefficient ε_{AAE} are selected to evaluate the Co-PCE and SRSM. The calculations of the two coefficients are as follows:

$$\varepsilon_{ARMS}=\sqrt{\frac{1}{M}\sum_{i=1}^{M}(\xi_{MC}(x_i)-\xi(x_i))^2} \tag{14}$$

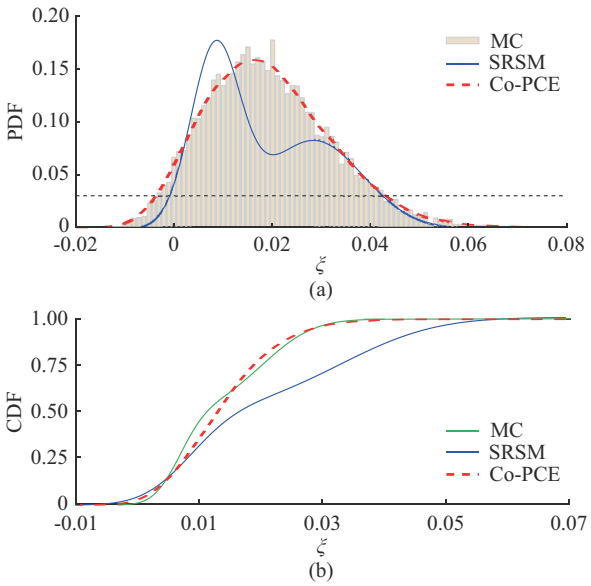

Fig. 11. PDF and CDF calculated by comparing Co-PCE, SRSM, and MC method. (a) PDF. (b) CDF.

$$\varepsilon_{AAE}=\frac{\sum_{i=1}^{M}\left|\xi_{MC}(x_i)-\xi(x_i)\right|}{M\cdot STD} \tag{15}$$

where $\xi_{MC}(x_i)$ is the damping ratio obtained by the MC method; $\xi(x_i)$ is the damping ratio sought by the method to be evaluated; M is the total number of sampling points; and STD is the standard deviation of the function values of the test sample points.

The evaluation results of different methods are shown in Table II. The 2nd-order SRSM shows the lowest accuracy, which is significantly lower than that of Co-PCE. The accuracy of the 3rd-order SRSM is improved but remains lower than that of Co-PCE. For SRSM, the choice of order has a great impact on the accuracy of the results. For Co-PCE, the order also affects the accuracy of the results, but high accuracy results are obtained with both orders.

TABLE II
EVALUATION RESULTS OF DIFFERENT METHODS

Method	Mean	Standard deviation (10^{-4})	ε_{ARMS}	ε_{AAE}	Time (s)
MC	0.02477	2.5621			8100.0
2nd-order SRSM	0.02685	2.4498	0.1152	0.1749	17.2
3rd-order SRSM	0.02366	2.5439	0.0671	0.0857	18.6
2nd-order Co-PCE	0.02582	2.5698	0.0091	0.0176	17.4
3rd-order Co-PCE	0.02479	2.5620	0.0057	0.0116	19.0

The statistical information and calculation time of the damping ratio with the three methods are also compared in Table II. The simulation result of the MC method can be used to judge the accuracy of Co-PCE and SRSM. The comparison shows that compared with the mean and standard deviation of Co-PCE, the results of SRSM are still less accurate. The main reason is that the true correlation is not con-

sidered. However, the calculation speed of SRSM is slightly faster than Co-PCE, and both methods result in a significant reduction in calculation time compared with the MC method.

2) Parameter Analysis and Optimization

The results of the damping response surface considering illumination intensity and load uncertainties based on BTBC interconnection are shown in Fig. 12. Specifically, when the illumination intensity is within the range of 0-200 W/m^2, an increase in the damping ratio is observed as the solar irradiance increases, resulting in the improved system stability.

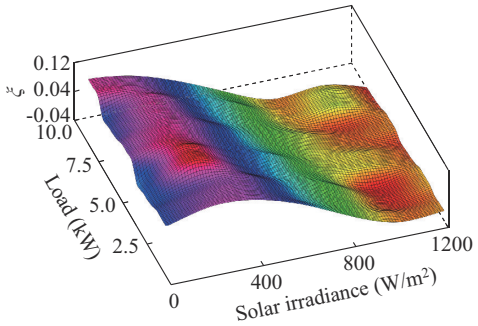

Fig. 12. Damping response surface considering illumination intensity and load uncertainties based on BTBC interconnection.

When the illumination intensity is within the range of 300-1000 W/m^2, a decrease in the damping ratio is observed as the illumination intensity increases. However, when the illumination intensity exceeds 1000 W/m^2, the damping ratio increases. Besides, it can be observed that the load has a low impact on the system stability. As the load increases, the damping ratio increases, and the system becomes more stable.

To identify the control parameters, a variance-based sensitivity analysis is conducted to determine which parameters are more sensitive to the dominant mode. Those parameters deemed to be insensitive are considered to cause relatively minor influence on damping. Accordingly, parameters that cause a more pronounced influence on damping are selected for examination of the damping response surface, as shown in Fig. 13. These parameters are C_ω, C_Q, $K_{i\mathrm{BP}}$, and $K_{i\mathrm{B}\alpha}$.

The stability margin of the control parameter stability region decreases as the parameters increase. However, if the parameter is set too small, some control performances may be lost. Therefore, the controllable variables (control parameters) and uncontrollable variables (wind speed, illumination intensity, etc.) are further combined to analyze the joint impact.

Taking C_ω and illumination intensity as example, Fig. 14 shows a damping response surface for control parameters against the backdrop of uncertain power output. The changes of control parameters and illumination intensity lead to the deterioration of damping. Consequently, the control parameters are optimized in the context of uncertain output. By optimizing the controllable variables, the system is ensured to retain small signal stability despite the uncertainties.

Based on the above parameter optimization method, the control parameters are optimized. Parameter values before and after optimization are shown in Table III.

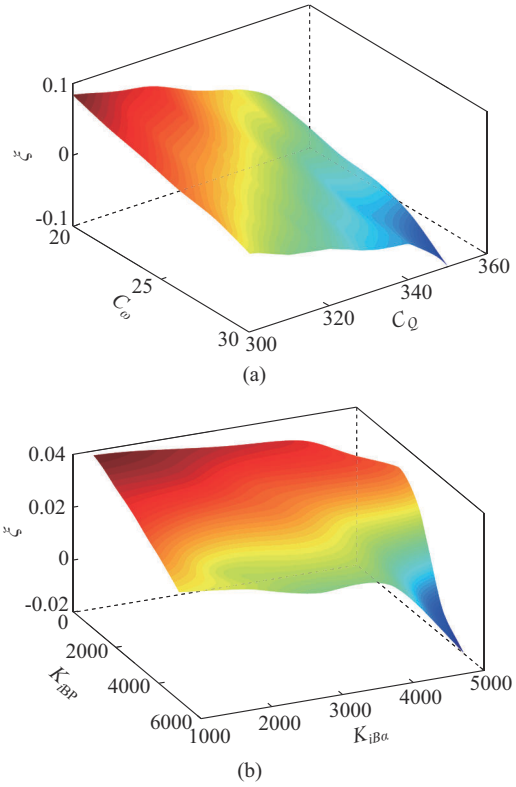

Fig. 13. Influence of different control parameters on damping response surface. (a) Control parameters of MG. (b) Control parameters of BTBC.

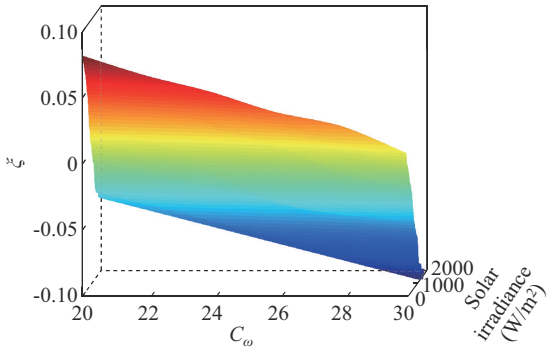

Fig. 14. Damping response surface for control parameters against backdrop of uncertain power output.

TABLE III
PARAMETER VALUES BEFORE AND AFTER OPTIMIZATION

Stage	C_ω	C_Q	$K_{i\mathrm{BP}}$	$K_{i\mathrm{B}\alpha}$
Before optimization	25	320	2000	2000
After optimization	10	200	4000	2000

The parameter optimization can effectively improve the system robustness by jointly adjusting control parameters and considering the stability of random small signals.

3) Effects of Different Interconnection Ways on System Stability

The stability characteristics of impedance interconnection and BTBC interconnection are analyzed when bidirectional power flows are present, and the influence of different inter-

connection ways on system stability is studied.

When the transmission power remains constant, the characteristic root distribution of impedance interconnection and BTBC interconnection is shown in Fig. 15. Due to the existence of multiple control links in the BTBC, the number of characteristic roots of BTBC interconnection increases, and the poles related to the BTBC are added based on the original characteristic roots.

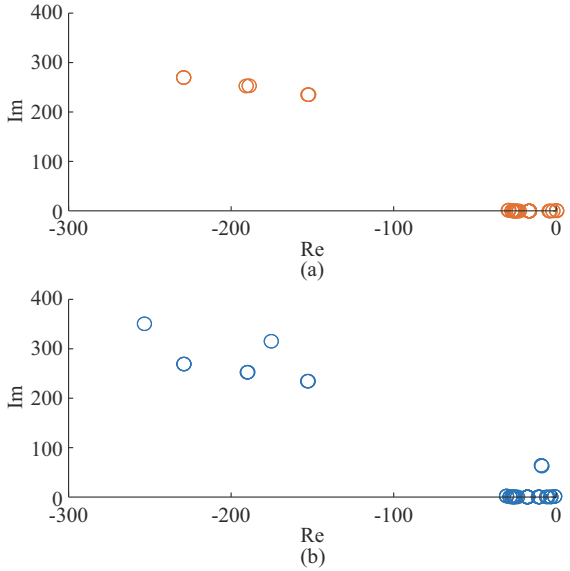

Fig. 15. Characteristic root distribution of impedance interconnection and BTBC interconnection. (a) Impedance interconnection. (b) BTBC interconnection.

The key mode damping ratios of the two interconnection ways are compared to evaluate the instability probability of this mode. Figure 16 shows the PDF and CDF results of the impedance interconnection. The instability probability of the impedance interconnection is 52.4%.

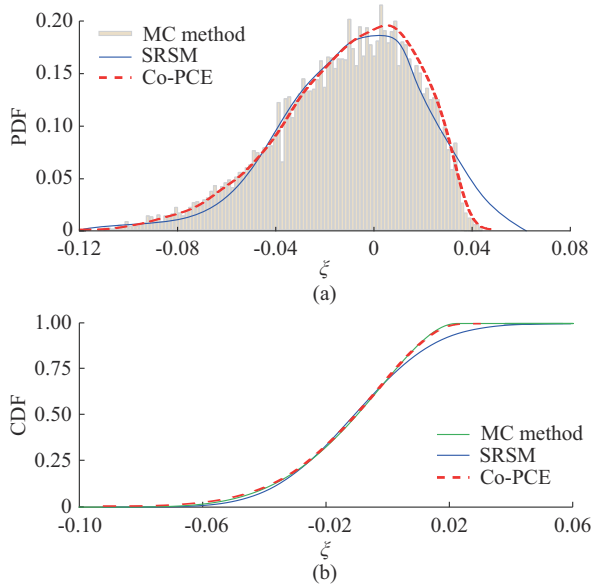

Fig. 16. PDF and CDF results of impedance interconnection. (a) PDF. (b) CDF.

This indicates that the instability probability of the BTBC interconnection is lower than that of the impedance interconnection. BTBC provides an isolation effect and can offset the impact of power fluctuations to a certain extent.

The damping response surface based on the impedance interconnection is shown in Fig. 17. Since the key mode damping ratio of the impedance interconnection is dominated by the state variables of MGs, the instability probability increases.

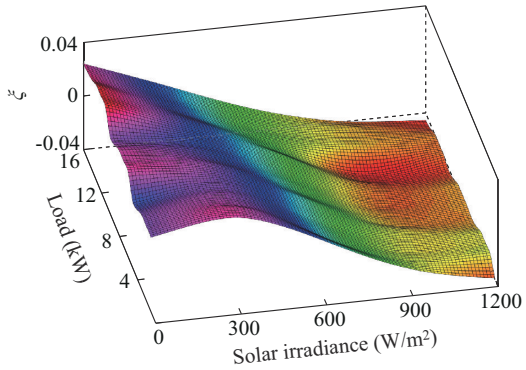

Fig. 17. Damping response surface based on impedance interconnection.

B. Effectiveness of Cooperative Control

1) Effectiveness Verification

To verify the effectiveness of the proposed cooperative control, a comparison of different controls is presented in Fig. 18, where $f_{\mathrm{DG1},i}$, $V_{\mathrm{oDG1},i}$, $\alpha_{\mathrm{DG1},i}$, and $\beta_{\mathrm{DG1},i}$ $(i=1,2,3,4,5)$ are the frequency, voltage, active power sharing ratio, and reactive power sharing ratio of DGs, respectively. The simulation results show the performance at three stages. Stage I is 0-8 s where only local droop control is performed. At 2 s, the frequency difference control of the BTBC is activated. Stage II is 8-16 s where distributed control is applied. The load is connected at 12 s. Stage III is 16-24 s where the active power sharing ratio control of BTBC is activated.

After the implementation of distributed control, the frequency of each DG in the MG is restored to 50 Hz. The output voltage is restored to the bounded output voltage. The active and reactive power sharing ratios of each DG remain the same. Objectives 1-4 are achieved. The active power sharing ratios of different MGs are illustrated in Fig. 19, which verify the effectiveness of achieving Objective 5. $\alpha_{\mathrm{MG}i}$ $(i=1,2,3)$ is the average active power sharing ratio of different MGs.

At 2-8 s, the frequency difference control of the BTBC can gradually converge the active power sharing ratios between MGs to the same value. However, after the distributed control is implemented in the MGs, the power transmission between MGs is seriously disturbed. At 12 s, the difference of the active power sharing ratios between the MGs changes and no longer converges to the same value. At 16 s, the active power sharing ratio control of the BTBC is performed. After 16 s, the active power sharing ratios between MGs converge to the same value again, and Objective 5 is achieved.

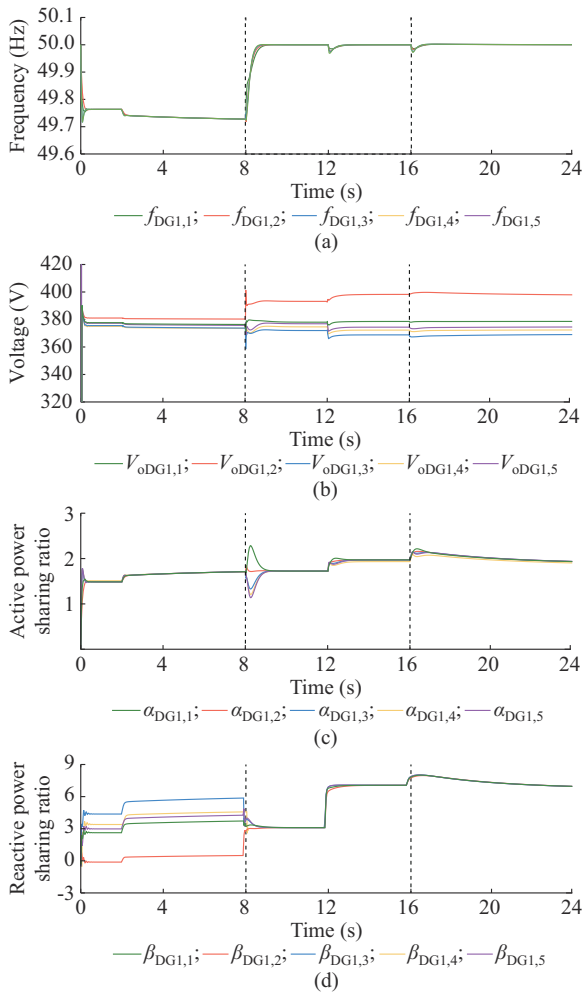

Fig. 18. Simulation results within MG with different controls. (a) Frequency. (b) Voltage. (c) Active power sharing ratio. (d) Reactive power sharing ratio.

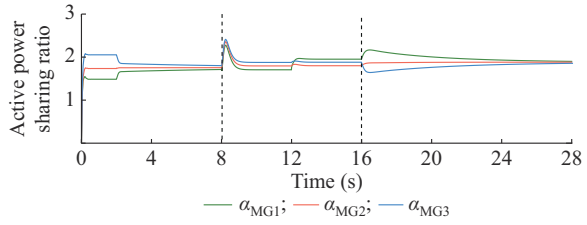

Fig. 19. Active power sharing ratios of different MGs.

2) Validation of Parameter Optimization

The analysis results from the parameter stability domain are employed to incorporate uncertainties in output into the settings of the cooperative control parameters, thereby enhancing the system robustness. Figure 20 shows the simulation results of the active power sharing ratios within the MG before and after the parameter optimization. It is evident that the active power sharing ratios demonstrate the improved control performance after the parameter optimization.

Figure 21 displays the simulation results of the active power sharing ratios of different MGs and the transmission power of the BTBC before and after the parameter optimization. After the parameter optimization, the effectiveness of both primary and secondary controls of the BTBC is enhanced. Furthermore, the time required to achieve active power sharing ratio control among MGs is reduced, and the amplitude of oscillations during secondary control is significantly diminished.

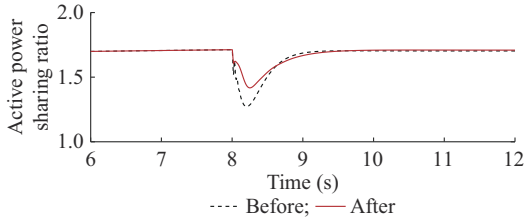

Fig. 20. Simulation results of active power sharing ratios within MG before and after parameter optimization.

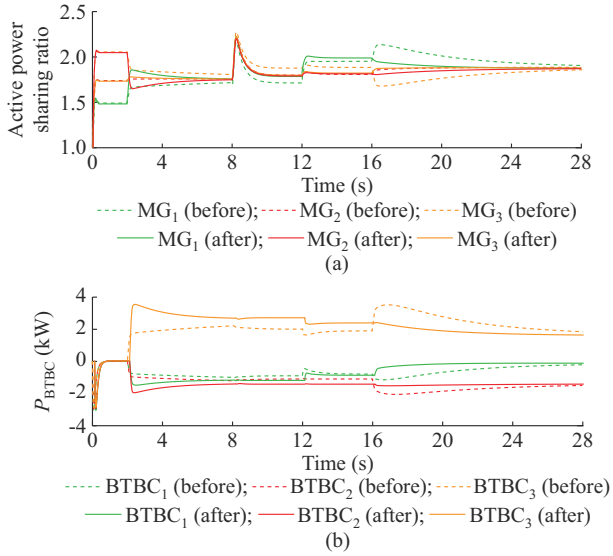

Fig. 21. Active power sharing ratios of different MGs and transmission power of BTBC before and after parameter optimization. (a) Active power sharing ratios. (b) Transmission power of BTBC.

VI. Conclusion

In this paper, a probabilistic small-signal stability assessment and cooperative control framework for BTBC-IMGs is proposed. The proposed framework improves the accuracy of frequency and voltage recovery control, and active power sharing ratio control. Subsequently, the effects of uncertain RES fluctuations and collaborative control on small-signal stability are investigated. The accuracy of the assessment method is verified in MATLAB/Simulink and compared with the MC method and SRSM. Parametric damping response surfaces considering the correlation modeling are investigated. On this basis, the control parameters are optimized under the random RES fluctuations, ensuring that BTBC-IMGs maintain precise control objectives despite the presence of uncertainty fluctuations. The robustness of BTBC-IMGs is effectively enhanced.

Appendix A

Since local droop control has inherent bias, based on the consistency algorithm, the distributed secondary control with-

in the MG is designed as follows.

The compensation value of the frequency recovery control $u_{\omega,ke}$ can be designed as:

$$u_{\omega,ke}=-C_{\omega,ke}\left[\sum_{h\in a}a_{eh}^{k}(\omega_{ke}-\omega_{kh})+g_{e}^{k}(\omega_{ke}-\omega_{\mathrm{ref}})\right] \quad \text{(A1)}$$

where $C_{\omega,ke}$ is the frequency compensation value gain, which is a positive value; a_{eh}^{k} is the adjacent weight from DG_{kh} to DG_{ke} in MG_{k}; ω_{ke} and ω_{kh} are the output angular frequencies of DG_{ke} and DG_{kh}, respectively; g_{e}^{k} is the weight value of the virtual node DG_{0} to DG_{ke} in MG_{k}; and ω_{ref} is the set frequency reference value.

The compensation value of the active power sharing control $u_{P,ke}$ can be designed as:

$$u_{P,ke}=-C_{P,ke}\sum_{h\in a}a_{eh}^{k}(m_{ke}P_{ke}-m_{kh}P_{kh}) \quad \text{(A2)}$$

where $C_{P,ke}$ is the active power compensation value gain, which is a positive value; m_{ke} and m_{kh} are the active power droop control coefficients of DG_{ke} and DG_{kh}, respectively; and P_{ke} and P_{kh} are the average active power of DG_{ke} and DG_{kh}, respectively.

The adjustment amount of the distributed frequency control $\Delta\Omega_{ke}$ is defined as:

$$\Delta\Omega_{ke}=u_{\omega,ke}+u_{P,ke} \quad \text{(A3)}$$

The value of the distributed frequency control is:

$$\omega_{ke}=\omega_{\mathrm{n},ke}-m_{ke}P_{ke}+\Delta\Omega_{ke} \quad \text{(A4)}$$

where $\omega_{\mathrm{n},ke}$ is the rated angular frequency.

The compensation value of the voltage recovery control can be designed as:

$$u_{v,ke}=-C_{v,ke}\left[\sum_{h\in a}a_{eh}^{k}(\hat{V}_{ke}-\hat{V}_{kh})+g_{e}^{k}(\hat{V}_{ke}-V_{\mathrm{ref}})\right] \quad \text{(A5)}$$

where $\hat{V}_{ke}$ and $\hat{V}_{kh}$ are the bounded output voltages of DG_{ke} and DG_{kh}, respectively; $C_{v,ke}$ is the voltage compensation value gain, which is a positive value; and V_{ref} is the bounded voltage reference value.

The compensation value of the reactive power control can be designed as:

$$u_{Q,ke}=-C_{Q,ke}\sum_{h\in a}a_{eh}^{k}(n_{ke}Q_{ke}-n_{kh}Q_{kh}) \quad \text{(A6)}$$

where $C_{Q,ke}$ is the reactive power compensation value gain, which is a positive value; n_{ke} and n_{kh} are the reactive power droop control coefficients of DG_{ke} and DG_{kh}, respectively; and Q_{ke} and Q_{kh} are the average reactive power of DG_{ke} and DG_{kh}, respectively.

The adjustment amount of distributed bounded voltage control $\Delta\Phi_{ke}$ is:

$$\Delta\Phi_{ke}=u_{v,ke}+u_{Q,ke} \quad \text{(A7)}$$

The value of distributed bounded voltage control is:

$$\begin{cases}v_{od,ke}=v_{\mathrm{n},ke}-n_{ke}Q_{ke}+\Delta\Phi_{ke}\\ v_{oq,ke}=0\end{cases} \quad \text{(A8)}$$

where $v_{od,ke}$ and $v_{oq,ke}$ are the output voltage amplitudes in the dq coordinate; and $v_{\mathrm{n},ke}$ is the rated voltage amplitude.

REFERENCES

[1] C. Chen, J. Wang, F. Qiu *et al*., "Resilient distribution system by microgrids formation after natural disasters," *IEEE Transactions on Smart Grid*, vol. 7, no. 2, pp. 958-966, Mar. 2016.

[2] V. B. Pamshetti, S. Singh, A. K. Thakur *et al.*, "Multistage coordination volt/var control with CVR in active distribution network in presence of inverter-based DG units and soft open points," *IEEE Transactions on Industry Applications*, vol. 57, no. 3, pp. 2035-2047, May 2021.

[3] M. Shahidehpour, Z. Li, S. Bahramirad *et al*., "Networked microgrids: exploring the possibilities of the IIT-Bronzeville grid," *IEEE Power and Energy Magazine*, vol. 15, no. 4, pp. 63-71, Jul. 2017.

[4] L. Qiao, X. Li, D. Huang *et al*., "Coordinated control for medium voltage DC distribution centers with flexibly interlinked multiple microgrids," *Journal of Modern Power Systems and Clean Energy*, vol. 7, no. 3, pp. 599-611, May 2019.

[5] T. T. Nguyen, H. J. Yoo, and H. M. Kim, "A droop frequency control for maintaining different frequency qualities in a stand-alone multimicrogrid system," *IEEE Transactions on Sustainable Energy*, vol. 9, no. 2, pp. 599-609, Apr. 2018.

[6] N. Bottrell, M. Prodanovic, and T. C. Green, "Dynamic stability of a microgrid with an active load," *IEEE Transactions on Power Electronics*, vol. 28, no. 11, pp. 5107-5119, Nov. 2013.

[7] Z. Zhao, P. Yang, Y. Wang *et al*., "Dynamic characteristics analysis and stabilization of PV-based multiple microgrid clusters," *IEEE Transactions on Smart Grid*, vol. 10, no. 1, pp. 805-818, Jan. 2019.

[8] X. Wu, C. Shen, and R. Iravani, "A distributed, cooperative frequency and voltage control for microgrids," *IEEE Transactions on Smart Grid*, vol. 9, no. 4, pp. 2764-2776, Jul. 2018.

[9] J. Liao, N. Zhou, Z. Qin *et al*., "Coordination control of power flow controller and hybrid DC circuit breaker in MVDC distribution networks," *Journal of Modern Power Systems and Clean Energy*, vol. 9, no. 6, pp. 1257-1268, Nov. 2021.

[10] J. L. Rueda, D. G. Colome, and I. Erlich, "Assessment and enhancement of small signal stability considering uncertainties," *IEEE Transactions on Power Systems*, vol. 24, no. 1, pp. 198-207, Feb. 2009.

[11] R. Cao, J. Xing, B. Sui *et al*., "An improved integrated cumulant method by probability distribution pre-identification in power system with wind generation," *IEEE Access*, vol. 9, pp. 107589-107599, Jul. 2021.

[12] Z. Lu, X. Xu, Z. Yan *et al*., "Density-based global sensitivity analysis of islanded microgrid load ability considering distributed energy resource integration," *Journal of Modern Power Systems and Clean Energy*, vol. 8, no. 1, pp. 94-101, Mar. 2020.

[13] M. Han, H. K. Lam, F. Liu *et al*., "Stability analysis and estimation of domain of attraction for positive polynomial fuzzy systems with input saturation," *IEEE Transactions on Fuzzy Systems*, vol. 28, no. 8, pp. 1723-1736, Aug. 2020.

[14] D. Shen, H. Wu, B. Xia *et al*., "Arbitrarily sparse polynomial chaos expansion for high-dimensional parametric problems: parametric and probabilistic power flow as an example," *IEEE Systems Journal*, vol. 16, no. 3, pp. 4950-4961, Sept. 2022.

[15] K. Ye, J. Zhao, N. Duan *et al*., "Stochastic power system dynamic simulation and stability assessment considering dynamics from correlated loads and PVs," *IEEE Transactions on Industry Applications*, vol. 58, no. 6, pp. 7764-7775, Nov. 2022.

[16] Y. Zhou, Y. Li, W. Liu *et al*., "The stochastic response surface method for small-signal stability study of power system with probabilistic uncertainties in correlated photovoltaic and loads," *IEEE Transactions on Power Systems*, vol. 32, no. 6, pp. 4551-4559, Nov. 2017.

[17] Y. Jiang, Z. Ren, Z. Sun *et al*., "A stochastic response surface method based probabilistic energy flow analysis method for integrated electricity and gas systems," *IEEE Transactions on Power Systems*, vol. 37, no. 3, pp. 2467-2470, May 2022.

[18] H. Palahalli, P. Maffezzoni, and G. Gruosso, "Gaussian Copula methodology to model photovoltaic generation uncertainty correlation in power distribution networks," *Energies*, vol. 14, no. 9, p. 2349, Apr. 2021.

[19] J. Xu, P. K. Kanyingi, K. Wang *et al*., "Probabilistic small signal stability analysis with large scale integration of wind power considering dependence," *Renewable and Sustainable Energy Reviews*, vol. 69, pp. 1258-1270, Mar. 2017.

[20] K. Ye, J. Zhao, Y. Zhang *et al*., "A generalized computationally efficient Copula-polynomial chaos framework for probabilistic power flow considering nonlinear correlations of PV injections," *International Journal of Electrical Power & Energy Systems*, vol. 136, p.

107727, Mar. 2022.
[21] K. N. Hasan and R. Preece, "Influence of stochastic dependence on small-disturbance stability and ranking uncertainties," *IEEE Transactions on Power Systems*, vol. 33, no. 3, pp. 3227-3235, May 2018.
[22] M. Andreasson, R. Wiget, D. V. Dimarogonas *et al*., "Distributed frequency control through MTDC transmission systems," *IEEE Transactions on Power Systems*, vol. 32, no. 1, pp. 250-260, Jan. 2017.
[23] A. Yogarathinam and N. R. Chaudhuri, "Stability-constrained adaptive droop for power sharing in AC-MTDC grids," *IEEE Transactions on Power Systems*, vol. 34, no. 3, pp. 1955-1965, May 2019.
[24] M. Naderi, Y. Khayat, Q. Shafiee *et al*., "An emergency active and reactive power exchange solution for interconnected microgrids," *IEEE Journal of Emerging and Selected Topics in Power Electronics*, vol. 9, no. 5, pp. 5206-5218, Oct. 2021.
[25] J. Zhou, H. Zhang, Q. Sun *et al*., "Event-based distributed active power sharing control for interconnected AC and DC microgrids," *IEEE Transactions on Smart Grid*, vol. 9, no. 6, pp. 6815-6828, Nov. 2018.
[26] M. J. Hossain, M. A. Mahmud, F. Milano *et al*., "Design of robust distributed control for interconnected microgrids," *IEEE Transactions on Smart Grid*, vol. 7, no. 6, pp. 2724-2735, Nov. 2016.
[27] X. Li, L. Guo, Y. Li *et al*., "A unified control for the DC-AC interlinking converters in hybrid AC/DC microgrids," *IEEE Transactions on Smart Grid*, vol. 9, no. 6, pp. 6540-6553, Nov. 2018.
[28] S. Koebrich, T. Bowen, and A. Sharpe, "2018 Renewable Energy Data Book: U. S. Department of Energy (DOE), Energy Efficiency & Renewable Energy (EERE)," National Renewable Energy Laboratory, Golden, CO, USA, 2020.

Yuhong Wang received the B.S. and M.S. degrees in power system and its automation from Chongqing University, Chongqing, China, in 1993 and 1995, respectively, and the Ph. D. degree in power system and its automation from Southwest Jiaotong University, Chengdu, China, in 2008. She is currently a Professor with Sichuan University, Chengdu, China. Her research interests include power system stability and control, high-voltage direct current (HVDC), renewable energy integration, and artificial intelligence.

Xinyao Wang received the B. E. degree in the College of Electrical Engineering from Sichuan University, Chengdu, China, in 2021. She is currently pursuing a Ph. D. degree at Sichuan University. Her research interests include power system stability and control, renewable energy integration, and HVDC transmission.

Jianquan Liao received the B. S. degree in electrical engineering from the China University of Petroleum, Qingdao, China, in 2017, and the Ph. D. degree from Chongqing University, Chongqing, China, in 2021. He has been an Associate Research Fellow with the School of Electrical Engineering, Sichuan University, Chengdu, China, since 2021. His current research interests include power system protection and control, power quality of DC distribution network, and power system stability and control.

Miaohong Su received the M. S. degree in the College of Electrical Engineering from Lanzhou Jiaotong University, Lanzhou, China, in 2021. She is currently pursuing the Ph.D. degree at Sichuan University, Chengdu, China. Her research interests include power system stability analysis and HVDC transmission.

Yongyue Liu received the B.E. degree in the School of Electrical and Information Engineering from Changsha University of Science and Technology, Changsha, China, in 2021. She is currently pursuing the M.S degree at Sichuan University, Chengdu, China. Her research interests include power system stability and control.